Vietnam Journal of Science and Technology ***58*** *(6) (2020) 718-727*

doi:10.15625/2525-2518/58/6/15157

HIGH PHOTOCATALYTIC ACTIVITY OF MAGNETIC COMPOSITE PHOTOCATALYST $NIFe_2O_4/BiVO_4$ FOR RHODAMINE B DEGRADATION UNDER VISIBLE LED LIGHT IRRADIATION

Minh Que Doan, Linh Xuan Nong, Trinh Duy Nguyen*

Center of Excellence for Green Energy and Environmental Nanomaterials (CE@GrEEN), Nguyen Tat Thanh University, 300A Nguyen Tat Thanh, District 4, Ho Chi Minh City, Viet Nam

*Email: *ndtrinh@ntt.edu.vn*

Received: 19 June 2020; Accepted for publication: 30 July 2020

Abstract. To improve the photocatalytic activity of $BiVO_4$ semiconductor, the design of composite photocatalyst containing $BiVO_4$ with surpassing the recombination of photoinduced electron and hole is highly required. In this study, magnetic composite photocatalyst with $NiFe_2O_4$ and $BiVO_4$ has developed through two-steps hydrothermal method. The results show that the morphology of the bare $BiVO_4$ had a decahedral shape with smooth surfaces along with particles, while the morphology of the bare $NiFeO_4$ had nanoparticles with the diameter in a range of 10 - 20 nm. In the case of 20 % $NiFe_2O_4/BiVO_4$ samples, a lot of nanoparticles were deposited into large bulk, implying the incorporation of $NiFe_2O_4$ nanoparticles on the surface of $BiVO_4$ catalyst. Compared with the bare $BiVO_4$, the $NiFe_2O_4/BiVO_4$ composites had a higher photocatalytic efficiency for photodecomposition of rhodamine B (RhB) under visible LED light irradiation. The improvement of photocatalytic degradation RhB activity should be attributed to a direct Z-scheme system. Therefore, the fabrication of semiconductors with a combination of magnetic materials provides new insight for the enhancement of their photocatalytic performance.

Keywords: magnetic composite photocatalyst, $NiFe_2O_4/BiVO_4$, rhodamine B degradation, visible LED light irradiation.

Classification numbers: 2.4.2, 2.6.1, 2.10.1.

1. INTRODUCTION

Advanced oxidation processes (AOPs) have been gained importance as promising approaches to treat emerging organic dyes in water media due to their advantage in the treatment of toxic and non-biodegradable persistent organic substances [1 - 3]. Primarily, AOPs can be classified under ozonation, sonolysis, homogeneous wet oxidation, ultraviolet irradiation, Fenton process or heterogeneous photocatalysis using semiconductors, radiolysis, and electrochemical methods. Among these techniques, a heterogeneous photocatalysis process is identified to have some advantages such as easy setup and operation at room temperatures. Besides, it is known as

an effective system for mineralization of organic dyes through the production of radicals into somewhat less persistent organic by-products, known as "green" chemicals, CO_2, and H_2O.

Semiconductor $BiVO_4$ has widely known to degrade organic dyes as they possess excellent stability and is environmentally friendly. Besides, $BiVO_4$ also possesses a narrow bandgap energy (2.4 eV), which can expose photocatalytic activity under visible light irradiation [4–7]. However, the photocatalytic performance of this material should be improved because of its slow charge transfer and low photo-generated charge carriers separation. These drawbacks could be surpassed by the design of $BiVO_4$ based on composite structure. For example, Pingmuang *et al*. [8] reported the synthesis of three composite photocatalysts containing $BiVO_4$ ($CeO_2/BiVO_4$, $TiO_2/BiVO_4$, and $WO_3/BiVO_4$), in which the prolongation of the lifetimes of photoexcited charges separation is considered as a critical factor to improve the photocatalytic activity of $BiViO_4$. The construction of the Z-scheme system with the combination of *p*-type $CaFe_2O_4$ and *n*-type $BiVO_4$ is capable of overall water splitting [9]. Nguyen *et al*. [10] reported that $Bi_2WO_6/BiVO_4$ nanocomposite exhibited high photocatalytic activity for the degradation of Rhodamine B under visible irradiation, which is due to the electron-hole recombination is restricted. The n-$BiVO_4$/p-Co_3O_4 composite stabilizes the photocurrent and enhances the efficiency of its generation, resulting in the compartmentalization of interfacial reduction and oxidation at the n-$BiVO_4$ and p-Co_3O_4, respectively [11]. $Ag_3PO_4/BiVO_4$ photocatalyst, prepared by in-situ precipitation router, exhibited higher photocatalytic activity in decomposition of rhodamine B and 2,4-dichlorophenol as comparison of the bare Ag_3PO_4 and $BiVO_4$ [12].

In this study, $NiFe_2O_4/BiVO_4$ composite was synthesized by two-steps hydrothermal method. The $NiFe_2O_4$ nanoparticles were first synthesized by the hydrothermal method and then were decorated on the surface of $BiVO_4$. The $NiFe_2O_4/BiVO_4$ composite was expected to exhibit a higher photocatalytic efficiency for photodecomposition of rhodamine B (RhB) under visible LED light irradiation as compared to that of the bare $BiVO_4$, owing to the complex structures and the incorporated magnetic species.

2. MATERIALS AND METHODS

2.1. Synthesis of catalysts

In our study, $Fe(NO_3)_3 \cdot 9H_2O$ (> 98 %) and $NiCl_2 \cdot 6H_2O$ (> 96 %) used as starting materials for the synthesis of $NiFe_2O_4$ powder were purchased from Fisher Chemical. $Bi(NO_3)_3 \cdot 5H_2O$ (ACS reagent, ≥ 98.0 %) and NH_4VO_3 used as starting materials for the synthesis of $BiVO_4$ powder were purchased from Sigma-Aldrich. In addition, KOH and HNO_3 were purchased from Xi Long Chemical.

We first prepared $NiFe_2O_4$ powder by the hydrothermal method. $Fe(NO_3)_3 \cdot 9H_2O$ (4 mmol) and $NiCl_2 \cdot 6H_2O$ (2 mmol) were dissolved in water (25 mL) to form a mixed solution. Then 25 mL of KOH 2.0 M was dropwise into the mixed solution and continuously stirred for 1 hour. The mixture was transferred into a 100 mL Teflon-lined autoclave and treated at 160 °C for 12 hours. After the reaction, the brownish-yellow precipitation was collected by centrifugation and cleaned with water and absolute ethanol, and finally dried at 60 °C for 48 h in a vacuum oven to obtain $NiFe_2O_4$ powder.

Magnetic composites x% $NiFe_2O_4/BiVO_4$ (where x is the weight ratio of $NiFe_2O_4/BiVO_4$ and was chosen as 0, 5, 10, 15, 20, and 25) were prepared by the hydrothermal method. Typically, four mmol of $Bi(NO_3)_3 \cdot 5H_2O$ were dispersed into 20 mL of HNO_3 2M. Next, four mmol of NH_4VO_3 was dissolved in 40 mL of hot water and stirred for 1 hour to obtain a

transparent solution. Then two solutions were mixed to form the yellow suspension. A certain amount of $NiFe_2O_4$ synthesized as described above was dispersed in the yellow suspension with vigorous stirring. After vigorously stirring for 30 minutes, the suspension was added into a 100 mL Teflon-lined autoclave and treated at 160 °C for 24 hours. The particles were harvested by centrifugation, washed with water and absolute ethanol, then dried under vacuum at 60 °C for 24 hours. Afterward, the obtained powder was calcined at 300 °C for 2 hours. For comparison, the bare $BiVO_4$ also was synthesized as the same method for the synthesis of $NiFe_2O_4/BiVO_4$ with the absence of $NiFe_2O_4$.

2.2. Instruments

The phase structures of magnetic composites x% $NiFe_2O_4/BiVO_4$ (or $NiFeO_4$ and $BiVO_4$ references) were characterized by powder X-ray diffraction patterns (XRD) using a D8 Advance Bruker power diffractometer. The UV–Visible diffuse reflectance spectra (UV–Vis DRS) of the products was recorded on a Hitachi U-4100 UV-vis-NIR spectrophotometer using $BaSO_4$ as the standard. The Brunauer–Emmett–Teller (BET) was evaluated by N_2 adsorption-desorption measurements with TriStar 3000 V6.07. The surface morphologies and chemical composition of samples were measured by field emission scanning electron microscope (SEM) using JEOL JSM-7600F equipped with Energy-dispersive X-ray spectroscopy (EDS) Oxford instruments 50 mm2 X-Max. The magnetic property of $NiFe_2O_4/BiVO_4$ was studied using a vibrating sample magnetometer (VSM, GMW 3474–140).

2.3. Photocatalytic activity test

The photodegradation of RhB over $NiFeO_4/BiVO_4$ composites (or $NiFeO_4$ and $BiVO_4$ references) was conducted under visible light irradiation (white LED lamp, 60 W). Typically, 0.2 g of $NiFe_2O_4/BiVO_4$ composite samples were dispersed into 300 mL of 10^{-5} M RhB solution in pyrex beaker. The suspension was mixed by a submersible water pump in the dark for 1 hour with capacity up to 300 L h^{-1} to reach the adsorption/desorption equilibrium. During illumination time, about 4 mL was withdrawed from the mixture and centrifuged to eliminate the small particle from the solution. The obtained solution was then determined of the concentration of RhB by Ultraviolet-Visible at wavelength $\lambda = 554$ nm.

3. RESULTS AND DISCUSSION

3.1. Crystal structure and morphological characteristics

The fabrication of $NiFe_2O_4/BiVO_4$ composite material underwent through two-steps hydrothermal method. The $NiFe_2O_4$ nanoparticles were first synthesized by the hydrothermal method and then were decorated on the surface of $BiVO_4$. The successful synthesis of these materials was verified by observing its morphology with SEM images. Figure 1 shows the SEM images of the $BiVO_4$ and $NiFe_2O_4$ and $NiFe_2O_4/BiVO_4$ composites. As shown in Figure 1, the morphology of the bare $BiVO_4$ had a decahedral shape with smooth surfaces along with small particles (Figure 1a), while the morphology of the bare $NiFeO_4$ had nanoparticles with the diameter in a range of 10 - 20 nm (Figure 1c). In the case of 20 % $NiFe_2O_4/BiVO_4$ samples, a large of nanoparticles were deposited into large bulk, implying the incorporation of $NiFe_2O_4$ nanoparticles on the surface of $BiVO_4$ catalyst. The EDS-Mapping analysis confirmed the chemical species of $NiFe_2O_4/BiVO_4$ composite and uniform distribution of Ni and Fe elements over the $BiVO_4$ surface (Figure 2d-i).

The XRD patterns of the $BiVO_4$ and $NiFe_2O_4$ and $NiFe_2O_4/BiVO_4$ composites are presented in Figure 2. The main peaks at 15.1°, 18.6°, 19.0°, 28.9°, 30.5°, 34.5°, 35.2°, 46.8°, and 47.2° were observed in $BiVO_4$ and $NiFe_2O_4/BiVO_4$ composites, which indicated the main phase of $BiVO_4$ is monoclinic scheelite [7, 13, 14]. The presence of $NiFe_2O_4$ nanoparticles in $NiFe_2O_4/BiVO_4$ composites was confirmed by the presence of main peaks at 30.2°, 35.6°, 43.3°, and 57.3° [15, 16]. Besides, the intensity of the peak at 35.6° increased along with the % mass composition of $NiFe_2O_4$ in composites. The lattice parameters for the $BiVO_4$ and $NiFe_2O_4/BiVO_4$ composites showed in Table 1 confirmed that the deposition of $NiFe_2O_4$ nanoparticles over the $BiVO_4$ surface did not significantly influence the crystal phase and structure of $BiVO_4$. These outcomes, along with SEM results, indicated the successful synthesis of $NiFe_2O_4/BiVO_4$ composites.

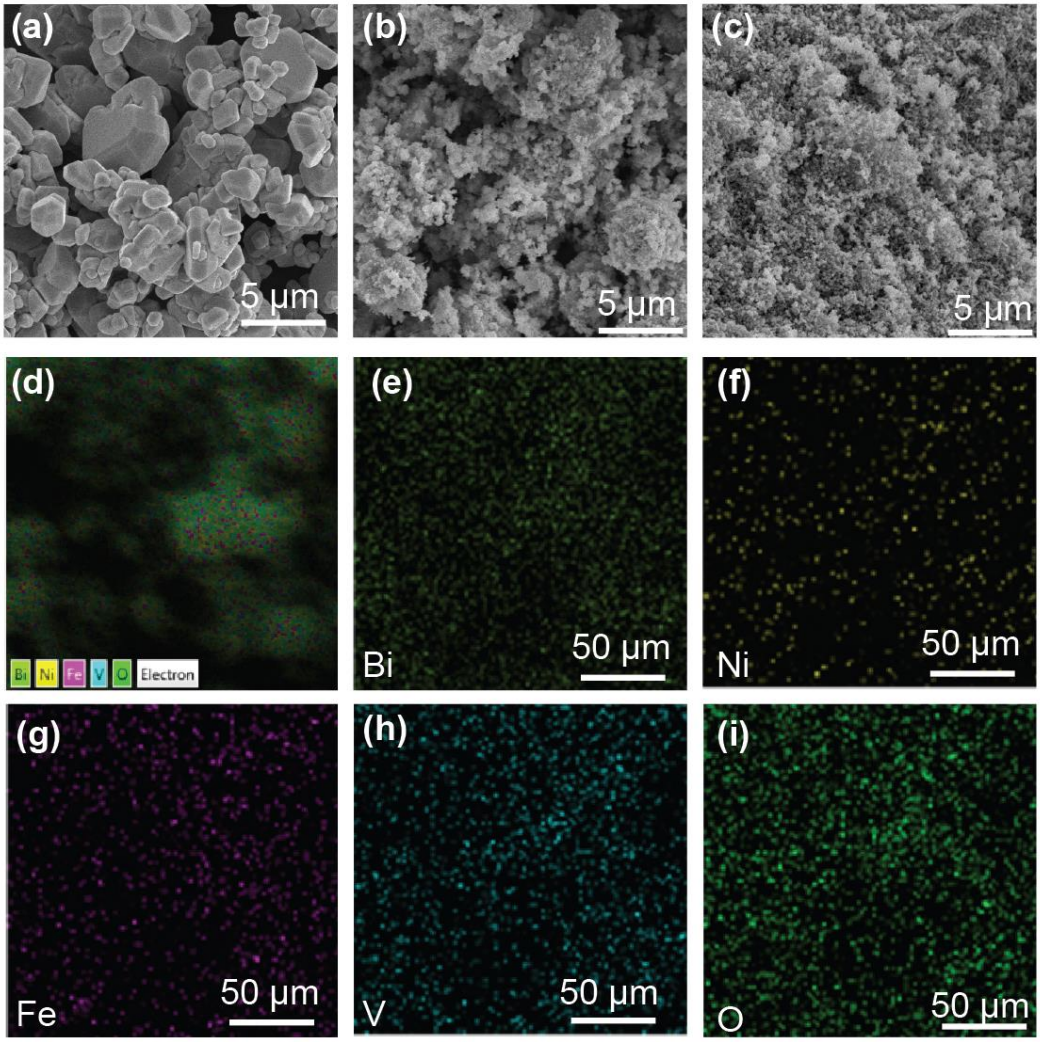

Figure 1. SEM images of pure $BiVO_4$ (a), 20 % $NiFe_2O_4/BiVO_4$ (b) and $NiFe_2O_4$ (c), and EDX spectra of 20 % $NiFe_2O_4/BiVO_4$ (d-i).

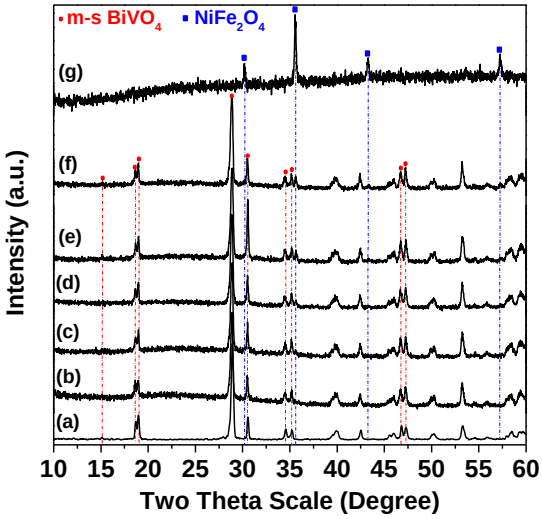

Figure 2. XRD patterns of $BiVO_4$ (a), 5% $NiFe_2O_4/BiVO_4$ (b), 10% $NiFe_2O_4/BiVO_4$ (c), 15 % $NiFe_2O_4/BiVO_4$ (d), 20 % $NiFe_2O_4/BiVO_4$ (e), 25 % $NiFe_2O_4/BiVO_4$ (f), and $NiFe_2O_4$ (g).

Table 1. The lattice parameters for the $BiVO_4$ and $NiFeO_4/BiVO_4$ composites.

Samples	Lattice parameters (Å)			β (°)	V (Å^3)
	a	b	c		
$BiVO_4$	5.18521	5.09312	11.69186	90.00998	309.7689
5 % $NiFe_2O_4/BiVO_4$	5.19920	5.09872	11.72061	90.14443	310.7039
10 % $NiFe_2O_4/BiVO_4$	5.19548	5.09788	11.70849	89.99217	310.1106
15 % $NiFe_2O_4/BiVO_4$	5.20148	5.09951	11.70617	90.01030	310.5063
20 % $NiFe_2O_4/BiVO_4$	5.19850	5.09823	11.69956	90.07130	310.0747
25 % $NiFe_2O_4/BiVO_4$	5.20177	5.09721	11.71897	90.11685	310.7223

The UV-Vis diffuse reflectance spectra and bandgap energies of the $NiFe_2O_4$, $BiVO_4$, and $NiFe_2O_4/BiVO_4$ nanocomposites are shown in Figure 3. As shown in Figure 3A, the absorption edge of bare $BiVO_4$ appears at around 550 nm, while $NiFe_2O_4$ has a great wider absorption in the visible light range. The absorption edge of $NiFe_2O_4/BiVO_4$ nanocomposites occurs in a range of 600 - 800 nm, implying that the absorption becomes higher than the bare $BiVO_4$ after the decoration of $NiFe_2O_4$ nanoparticles. The bandgap energy (E_g, eV) of all samples was estimated through Tauc plot method [17, 18]:

$$(\alpha.h\nu)^2 = A(h\nu - E_g) \quad (1)$$

where, α is the absorption coefficient, hν is the incident photon energy, and A is an energy independent constant. The bandgap values of $NiFe_2O_4$, $BiVO_4$, and $NiFe_2O_4/BiVO_4$ nanocomposites are shown in Table 2. The E_g value decreases with increasing $NiFe_2O_4$ content.

The conduction band (E_{CB}) and valence band (E_{VB}) of $NiFe_2O_4$ and $BiVO_4$ can be estimated by the formula [19,20]:

$$E_{CB} = \chi - E_o + 0.5E_g \quad (2)$$

$$E_{VB} = E_g - E_{CB} \quad (3)$$

where χ is the absolute electronegativity, χ is 6.04 eV and 5.84 eV for $BiVO_4$ and $NiFe_2O_4$, respectively [19,20]. E_o (4.5 eV) is the energy of free electrons on the hydrogen scale. The E_{CB} and E_{VB} value of $BiVO_4$ are 2.68 and 0.40 eV, respectively. The E_{CB} and E_{VB} values of $NiFe_2O_4$ are 1.73 and 0.17 eV, respectively.

Table 2. Physicochemical properties and chemical composition of $NiFe_2O_4/BiVO_4$ sample.

Sample	E_g (eV)	k_{app} (10^{-3} min^{-1})	R^2
NiFe2O4	1.56	0.596	0.90104
5 % $NiFe2O4/BiVO_4$	2.07	19.837	0.96008
10 % $NiFe2O4/BiVO_4$	1.69	20.547	0.94496
15 % $NiFe2O4/BiVO_4$	1.60	17.280	0.96941
20 % $NiFe2O4/BiVO_4$	1.57	25.430	0.97114
25 % $NiFe2O4/BiVO_4$	1.57	12.759	0.96681
$BiVO_4$	2.28	12.421	0.94266

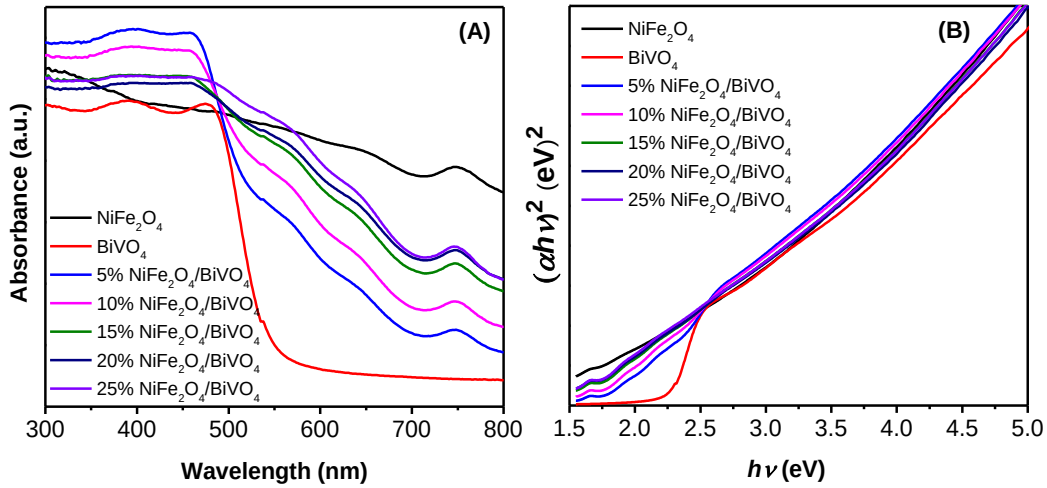

Figure 3. UV-vis diffuse reflectance spectra (a) and bandgap energies (b) of the $NiFe_2O_4$, $BiVO_4$ and $NiFe_2O_4/BiVO_4$ nanocomposites.

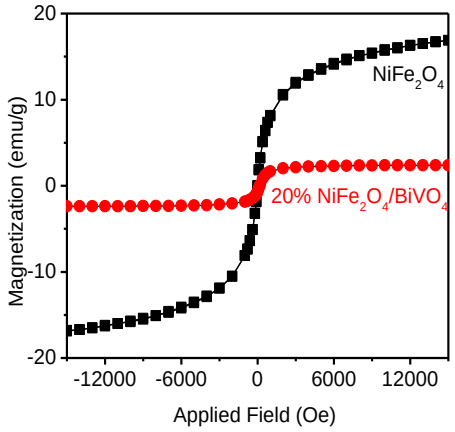

Figure 4. Magnetic properties of the $NiFe_2O_4$ and 20 % $NiFe_2O_4/BiVO_4$ nanocomposite.

Magnetic properties of the $NiFe_2O_4$ and $NiFe_2O_4/BiVO_4$ nanocomposite were also investigated. As shown in Figure 4, the saturation magnetization (M_s, emu/g) of the $NiFe_2O_4$ and 20 % $NiFe_2O_4/BiVO_4$ nanocomposites is 17.07 and 2.56 emu/g, respectively. The M_s value of 20 % $NiFe_2O_4/BiVO_4$ is lower than that of $NiFe_2O_4$, which is due to the presence of non-magnetic $BiVO_4$. The significant magnetization of the composite can be benefited for catalysts recovery after photocatalytic reaction by using an external magnetic field.

3.2. Photocatalytic performance

We investigated the photocatalytic performances of $NiFe_2O_4/BiVO_4$ composites along with $NiFe_2O_4$ and $BiVO_4$ through photodegradation of RhB under LED light irradiation. As shown in Figure 5A, RhB could rarely be degraded in the absence of catalyst during 6 h of LED light irradiation, suggesting the direct photolysis of RhB was negligible. As also shown in Figure 5A, $NiFe_2O_4/BiVO_4$ composites showed much higher photocatalytic activity than the bare $NiFe_2O_4$ and $BiVO_4$, indicating that the incorporation of $NiFe_2O_4$ nanoparticles could enhance the activity of $BiVO_4$ photocatalyst. The 20 % $NiFe_2O_4/BiVO_4$ possessed the best degradation ability RhB, with 82.9 % of RhB eliminated within 6 h of irradiation. The degradation kinetic through ln (C_o/C) versus irradiation time using a pseudo-first-order reaction rate for RhB was presented in Figure 5B. The apparent rate constants (k_{app}, min^{-1}) of 20 % $NiFe_2O_4/BiVO_4$ composite for RhB degradation were 25.430×10^{-3} min^{-1}, which is two times higher than that of pure $BiVO_4$. The difference in k_{app} values between $NiFe_2O_4/BiVO_4$ composite and $BiVO_4$ might be linked to their molecular structures and degradation mechanisms. Figure 5C exhibits the temporal evolution of the absorption spectra upon adsorption and with LED white light over $NiFe_2O_4/BiVO_4$ nanocomposites. The adsorption/desorption equilibrium between RhB molecules and $NiFe_2O_4/BiVO_4$ surface was reached after 1 h stirring in the dark. During irradiation, the broad UV-vis adsorption band 554 nm gradually decreased, and this peak shifted gradually to a shorter wavelength, implying the step-by-step degradation of RhB.

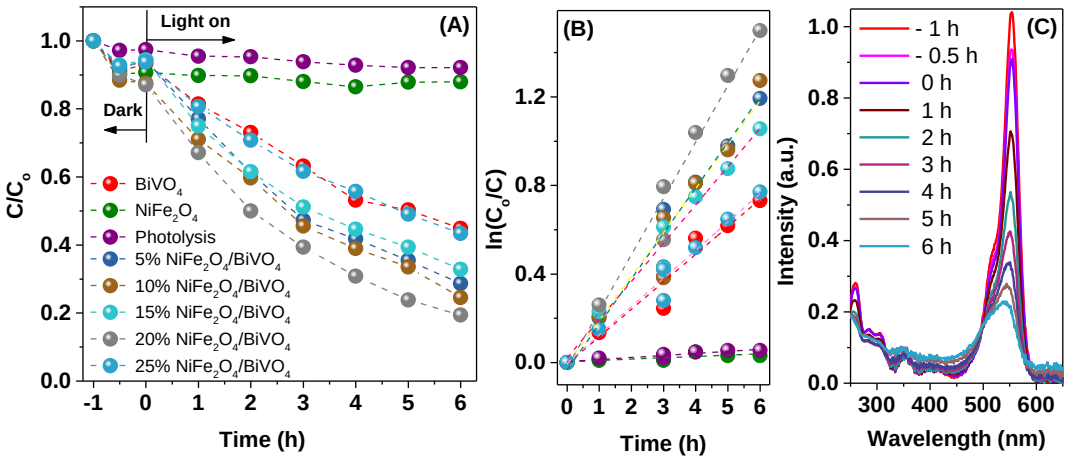

Figure 5. Photocatalytic activity of $NiFe_2O_4$, $BiVO_4$ and $NiFe_2O_4/BiVO_4$ nanocomposites through degrading RhB (A), degradation kinetic through ln (C_o/C) versus irradiation time using a pseudo-first-order reaction rate for RhB (B), the temporal evolution of the absorption spectra during the RhB photodegradation over $NiFe_2O_4/BiVO_4$ nanocomposites (C).

The suggested mechanism of photodegradation of RhB by $NiFe_2O_4/BiVO_4$ nanocomposite was

illustrated in Figure 6. In the RhB photodegradation over $NiFe_2O_4/BiVO_4$ nanocomposites, the photo-excited electrons (e^-) at CB of $NiFe_2O_4$ can migrate to the CB of $BiVO_4$, while the photo-excited holes (h^+) at VB of $BiVO_4$ can migrate to VB of $NiFe_2O_4$. As a result, thank to these transfers between $NiFe_2O_4$ and $BiVO_4$, the recombination of e^-/ h^+ pairs was restricted, which is corresponding to the enhancement of photocatalytic reaction. The h^+ can react with H_2O or OH^- to form hydroxyl radicals (OH*), while e^- can react with O_2 to form superoxide anion radical (O_2^{*-}). The radicals were shown to be a critical factor for the photocatalytic oxidation reaction, which can oxidize the RhB molecules to produce CO_2 and H_2O.

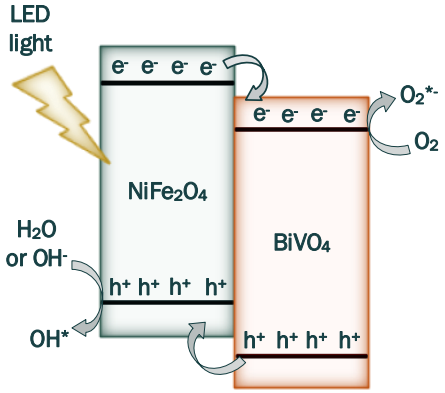

Figure 6. The suggested mechanism of photodegradation of RhB by $NiFe_2O_4/BiVO_4$ nanocomposite.

4. CONCLUSIONS

We successfully synthesized $NiFe_2O_4/BiVO_4$ nanocomposites through two-steps hydrothermal method. The results showed that the morphology of the bare $BiVO_4$ had a decahedral shape with smooth surfaces along with particles, while the morphology of the bare $NiFe_2O_4$ had nanoparticles with the diameter in a range of 10 - 20 nm. In the case of 20 % $NiFe_2O_4$/ $BiVO_4$ samples, a lot of nanoparticles particles were deposited into large bulk, implying the incorporation of $NiFe_2O_4$ nanoparticles on the surface of $BiVO_4$ catalyst. The EDS-Mapping analysis confirmed the chemical species of $NiFe_2O_4/BiVO_4$ composite and uniform distribution of Ni and Fe elements over the $BiVO_4$ surface. Compared with the bare $BiVO_4$, the $NiFe_2O_4/BiVO_4$ composites had a higher photocatalytic efficiency for photodecomposition of rhodamine B (RhB) under visible LED light irradiation. Besides, the 20 % $NiFe_2O_4/BiVO_4$ possessed the best degradation ability for RhB, i.e. with 82.9 % of RhB eliminated within 6 h of irradiation. The improvement of photocatalytic degradation RhB activity should be attributed to a direct Z-scheme system. Therefore, the fabrication of semiconductors with a combination of magnetic materials provide new insight for the enhancement of their photocatalytic performance.

ACKNOWLEDGEMENTS. THIS RESEARCH IS FUNDED BY VIETNAM NATIONAL FOUNDATION FOR SCIENCE AND TECHNOLOGY DEVELOPMENT (NAFOSTED) UNDER GRANT NUMBER 104.05-2017.315.

REFERENCES

1. Rivera-Utrilla J., Ocampo-Perez R., Sanchez-Polo M., Lopez-Penalver J. J., Gomez-Pacheco, C.V. - Removal of Tetracyclines from Water by Adsorption/Bioadsorption and Advanced Oxidation Processes. A Short Review, Curr. Org. Chem. **22** (2018) 1005-1021.

2. Klavarioti, M., Mantzavinos, D., Kassinos, D. - Removal of residual pharmaceuticals from aqueous systems by advanced oxidation processes., Environ. Int. **35** (2009) 402-17.
3. Saeid, S., Tolvanen, P., Kumar, N., Eränen, K., Peltonen, J., Peurla, M., Mikkola, J.P., Franz, A., Salmi, T. - Advanced oxidation process for the removal of ibuprofen from aqueous solution: A non-catalytic and catalytic ozonation study in a semi-batch reactor, Appl. Catal. B Environ. **230** (2018) 77-90.
4. Tan, G., Zhang, L., Ren, H., Wei, S., Huang, J., Xia, A. - Effects of pH on the hierarchical structures and photocatalytic performance of $BiVO_4$ powders prepared via the microwave hydrothermal method, ACS Appl. Mater. Interfaces **5** (2013) 5186-5193.
5. Xu T., Zhu R., Zhu G., Zhu J., Liang X., Zhu Y., He H. - Mechanisms for the enhanced photo-Fenton activity of ferrihydrite modified with $BiVO_4$ at neutral pH, Appl. Catal. B Environ. **212** (2017) 50-58.
6. Walsh A., Yan Y., Huda M. N., Al-Jassim M. M., Wei S. H. - Band edge electronic structure of $BiVO_4$: Elucidating the role of the Bi s and V d orbitals, Chem. Mater. **21** (2009) 547-551.
7. Ge M., Liu L., Chen W., Zhou Z. - Sunlight-driven degradation of Rhodamine B by peanut-shaped porous $BiVO_4$ nanostructures in the H_2O_2-containing system, CrystEngComm. **14** (2012) 1038-1044.
8. Pingmuang K., Chen J., Kangwansupamonkon W., Wallace G. G., Phanichphant S., Nattestad A. - Composite Photocatalysts Containing $BiVO_4$ for Degradation of Cationic Dyes, Sci. Rep. **7** (2017) 8929.
9. Srinivasan N., Sakai E., Miyauchi M. - Balanced Excitation between Two Semiconductors in Bulk Heterojunction Z-Scheme System for Overall Water Splitting, ACS Catal. **6** (2016) 2197-2200.
10. Dang Phu N., Huy Hoang L., Guo P. C., Chen X. B., Ching Chou W. - Study of photocatalytic activities of $Bi_2WO_6/BiVO_4$ nanocomposites, J. Sol-Gel Sci. Technol. **83** (2017) 640-646.
11. Long, Cai, Kisch H. - Visible Light Induced Photoelectrochemical Properties of n-$BiVO_4$ and n-$BiVO_4$/p-Co_3O_4, J. Phys. Chem. C **112** (2008) 548-554.
12. Qi X., Gu M., Zhu X., Wu J., Wu Q., Long H., He K. - Controlled synthesis of $Ag_3PO_4/BiVO_4$ composites with enhanced visible-light photocatalytic performance for the degradation of RhB and 2, 4-DCP, Mater. Res. Bull. **80** (2016) 215-222.
13. Tan H. L., Wen X., Amal, R., Ng Y. H. - $BiVO_4$ {010} and {110} Relative Exposure Extent: Governing Factor of Surface Charge Population and Photocatalytic Activity, J. Phys. Chem. Lett. **7** (2016) 1400-1405.
14. Wang D., Jiang H., Zong X., Xu Q., Ma Y., Li G., Li C. - Crystal facet dependence of water oxidation on $BiVO_4$ sheets under visible light irradiation, Chem. - A Eur. J. **17** (2011) 1275-1282.
15. Zhu P., Liu S., Xie J., Zhang S., Cao G., Zhao X. - Facile Synthesis of $NiFe_2O_4$/Reduced Graphene Oxide Hybrid with Enhanced Electrochemical Lithium Storage Performance, J. Mater. Sci. Technol. **30** (2014) 1078-1083.
16. Chen L., Dai H., Shen Y., Bai J. - Size-controlled synthesis and magnetic properties of $NiFe_2O_4$ hollow nanospheres via a gel-assistant hydrothermal route, J. Alloys Compd. **491** (2010) 33-38.

17. Asgari Moghaddam H., Jafari S., Mohammadi M. R. - Enhanced efficiency of over 10% in dye-sensitized solar cells through C and N single- and co-doped TiO_2 single-layer electrodes, New J. Chem. **41** (2017) 9453-9460.
18. Nguyen T. D., Bui Q. T. P., Le T. B., Altahtamouni T. M., Vu K. B., Vo D. V. N., Le N. T. H., Luu T. D., Hong S. S., Lim K. T. - Co^{2+} substituted for Bi^{3+} in $BiVO_4$ and its enhanced photocatalytic activity under visible LED light irradiation, RSC Adv. **9** (2019) 23526-23534.
19. Jiang H. Qing, Endo H., Natori H., Nagai M., Kobayashi K. - Fabrication and photoactivities of spherical-shaped $BiVO_4$ photocatalysts through solution combustion synthesis method, J. Eur. Ceram. Soc. **28** (2008) 2955-2962.
20. Sun J., Chen G., Wu J., Dong H., Xiong G. - Bismuth vanadate hollow spheres: Bubble template synthesis and enhanced photocatalytic properties for photodegradation, Appl. Catal. B Environ. **132**–**133** (2013) 304-314.